Gradient bundle analysis of ketosteroid isomerase (preprint copy)

Timothy R. Wilson[1], Amanda Morgenstern[2], Anastassia Alexandrova[3], and M.E. Eberhart[1,a]

[1]*Department of Chemistry, Colorado School of Mines*
[2]*Department of Chemistry & Biochemistry, UCCS*
[3]*Department of Chemistry, UCLA*
[a]*Corresponding author. Email: meberhar@mines.edu*

May 2, 2022

Abstract

Bond bundle analysis is used to investigate enzymatic catalysis in the KSI active site. We identify the unique bonding regions in each system and calculate the precise redistribution of electron density that accompanies either enhancement or inhibition of KSI catalytic activity. In two examples—using direct inspection of bond bundle regional properties, and using correlations between those properties and reaction barrier height—we arrive at similar conclusions, that catalytic enhancement results from promoting electron density redistribution between bonds within the KSI-docked substrate molecule in a way that closely resembles our mechanistic understanding of the forward catalyzed reaction. This catalyzing charge redistribution is prevalent in KSI systems catalyzed via electric fields or via amino acid mutation, and are thus suggestive of a significant catalytic role. Bond bundle analysis also generates a wealth of statistically useful bond properties, making it a strong candidate for machine learning approaches to computer-aided artificial enzyme design, and a promising tool for the discovery of relationships between the structure of the electron charge density and enzymatic catalytic activity.

Keywords: *bond bundle, bond wedge, gradient bundle analysis, gradient bundle decomposition, KSI, enzymatic catalysis, enzyme design, electron density analysis, QTAIM*

1 Introduction

Enzymes are biological macromolecules that accelerate chemical reactions by orders of magnitude. Cultivating an understanding of the mechanisms responsible for this process is a necessary step in the quest to synthesize efficient artificial enzymes. The past decades have been especially fruitful in this regard thanks to two significant advances: i) increasingly accurate structural studies; and ii) improved computational platforms and methods that allows us to predict, among other things, the conformation and energy of folded proteins and the reaction dynamics at enzyme active sites. In addition, these advances generate massive amounts of experimental and theoretical data that has proved effective in the search for statistical correlations to serve as parameters in the predictive

models generated with machine learning algorithms. To some degree overlooked, however, this wealth of data can also be used to identify new structures and structure-property relationships that may, in turn, be incorporated into the existing chemical formalisms, known collectively as chemical intuition. We believe that such structure-property relationships—models that can fit in a researcher's head—will be essential tools in the pursuit of enzyme design.

Here we demonstrate the applicability of one such tool through an investigation into the causes and effects of electrostatic preorganization [1–4]. Electrostatic preorganization is a strong, non-uniform external electric field (EEF) inherent to the arrangement and composition of amino acids about the active site. Only recently have accurate assessments of electrostatic preorganization become computationally feasible, with researchers now exploring available methods for such assessments. Meanwhile, the effects of applied electric fields on chemical reactivity have been experimentally and computationally observed for a variety of chemical reactions [5–24], many of which are also catalyzed enzymatically. Hence the specific problem of electrostatic preorganization, and the general problem of electric field catalysis, are of interest to enzymologists. Specifically, we provide support for the broader application of our tool by using it to study the model ketosteroid isomerase (KSI) system, the focus of numerous experimental and computational investigations (see Reference 25 for additional references), and build upon previous work elucidating the local structure underlying KSI's catalytic activity and how that activity can be augmented or hindered [25–27].

The tool used in this investigation, called bond bundle analysis, reduces a system to a set of chemical bonding regions whose energy, extent, electron count, and many other properties can be accurately calculated [28, 29]. In organic systems, understood using valence bond theory, bond bundle analysis often leads to chemically expected conclusions, but with a level of precision and generality not attainable through conventional methods [22, 27, 29].

This two-part investigation proceeds first with a direct inspection of bond bundle property distributions in the KSI active site in the presence and absence of a uniform EEF known to enhance its catalytic activity. In its second part, a set of KSI systems with varying catalytic activity is explored. The investigation reveals the redistribution of electron charge density, $\rho(\boldsymbol{r})$, between bonds that facilitates the forward reaction direction, and locates the active-site regions that most strongly correspond to catalytic enhancement or inhibition. Significantly, bond bundle analysis allows us to frame our finding within the language and concepts of chemical bonding. This framing leverages, informs, and quantifies many traditionally qualitative chemical concepts. It is this capability that

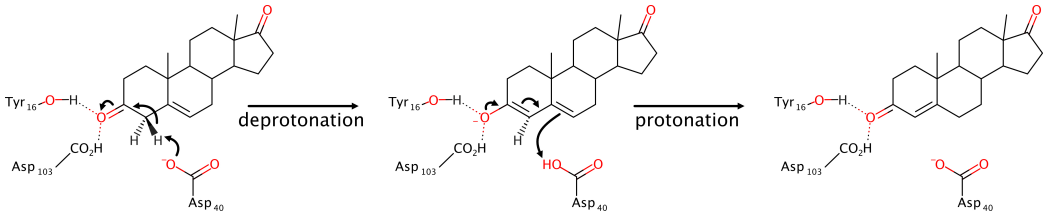

Scheme 1: Steroid isomerization reaction catalyzed by KSI.

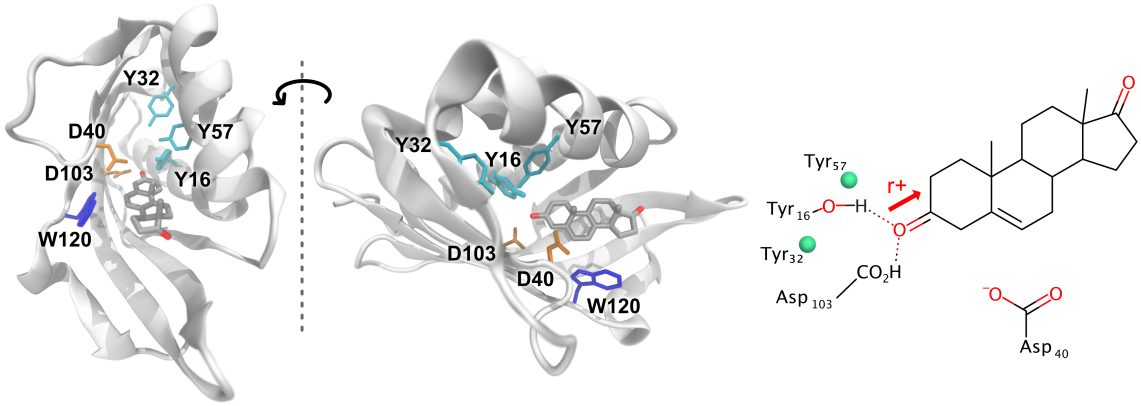

Figure 1: The full KSI protein (PDB code 1O10 [34]) with docked steroid substrate shown from two angles. The tyrosine (Y or Tyr; cyan), aspartic acid (D or Asp; orange) and tryptophan (W or Trp; blue) residues included in the small scale calculation are shown relative to the substrate (colored by element). The Lewis diagram of the system is shown with the "locations" of the 3-chlorotyrosine for the KSI variant systems (Trp_{120} not shown).

makes bond bundle analysis a promising part of the chemist's tool kit.

2 Background

2.1 Ketosteroid isomerase

The well-studied steroid isomerization reaction that KSI catalyzes involves the repositioning of a double C=C bond in the steroid substrate [25, 26, 30–33]. As shown in Scheme 1, this occurs by the removal of a proton from the secondary β-carbon, which is redeposited at the adjacent secondary carbon. Focusing on the first step, deprotonation is typically pictured as the result of a shift of charge though the substrate π system from the β-carbon to the carbonyl oxygen. In KSI this concerted atomic and electronic rearrangement is facilitated by the ideal positioning of Asp_{40}, providing a general base to receive the proton, and by the oxyanion hole that activates the carbonyl and stabilizes the charged enolate intermediate state.

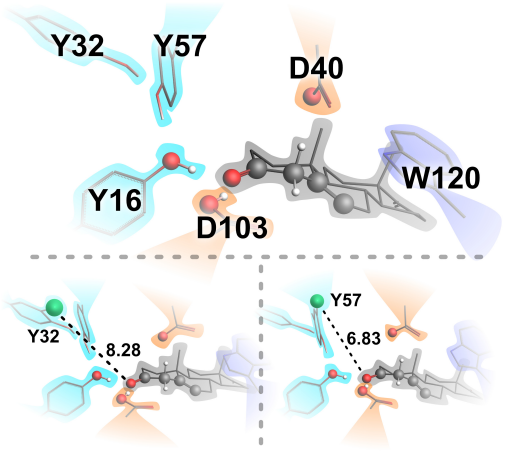

Figure 2: Closer depiction of the arrangement of amino acids forming the "oxyanion hole" about the substrate in KSI (top) and the positioning of the 3-chlorotyrosines in the KSI mutants (bottom) with Cl$\cdots$O1 distance (Å) indicated.

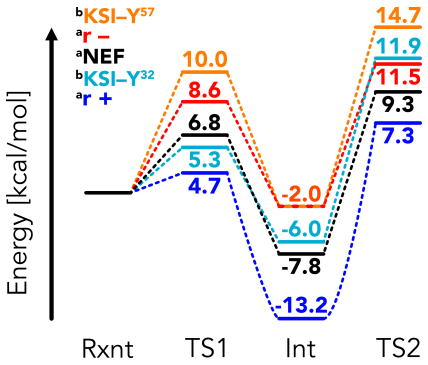

Figure 3: Reaction profiles for the systems in this study. Ordering at top-left is the same as in the TS1 column. [a]Data for the NEF and EEF systems taken from Fuller *et al.* [26]. [b]Data for KSI–Y systems taken from Hennefarth and Alexandrova [25].

Fuller *et al.* investigated the effects of applied EEFs to this process using the small-scale KSI active site shown in Figure 1, and found that a field applied parallel to the substrate carbonyl bond, pointing from O to C, augmented the electrostatic preorganization, lowering the reaction barrier, while a field in the opposite direction had the opposite effect [26]. This agrees with classical intuition, that an EEF should push charge opposite the field direction, in this case combining constructively with the KSI oxyanion hole to more readily shift charge to the carbonyl oxygen—further stabilizing the enolate intermediate state—and away from the β carbon, increasing its acidity and thus facilitating deprotonation.

Hennefarth and Alexandrova were then able to show similar reaction barrier effects in KSI variants that had a tyrosine mutated to a 3-chlorotyrosine [25]. Because the tyrosines of interest are involved in the extended hydrogen bonding network around the oxyanion hole (see Figure 2), this affects carbonyl activation, altering electrostatic preorganization. They found that a mutated Tyr_{32} lowered the barrier, and a mutated Tyr_{57} raised the barrier relative to the wild enzyme.

The present investigation uses the small-scale KSI active site, EEF directions, and 3-chlorotyrosine KSI variants from References 25 and 26 as the starting point for our calculations, and we explicitly use the same calculated reaction barrier energies. The five systems: wild KSI (a.k.a. NEF: no electric field), KSI^{r+} KSI^{r-} KSI-Y^{32} and KSI-Y^{57} provide a minimum example set of KSI enhancement

and inhibition via global and local perturbations; oriented EEFs in one case, and amino acid atomic substitution on the other. The regional changes in charge density and energy underlying the reaction barrier shifts should be accessible using this limited sample.

2.2 Assessing the local charge density origins of KSI catalytic enhancement

A common approach in the search for *local* relationships between $\rho(\boldsymbol{r})$ energy related catalytic properties (reaction barriers) is to seek correlations between the property of interest and charge density measures about points, lines, or within arbitrarily defined volumes. This approach has been employed to better understand the enhancement and inhibition mechanisms of KSI [25, 26].

Fuller *et al.* checked for correlations between KSI-catalyzed reaction barrier shifts due to EEFs and a number of local properties, such as interatomic distances and values of $\rho(\boldsymbol{r})$ at bond critical points (CPs) [26]. The strongest correlation found was that of the O2–H1 bond length,[1] which correlated positively with the change in reaction barrier, while the value of $\rho(\boldsymbol{r})$ at the corresponding bond CP anti-correlated, indicating that direct facilitation of the deprotonation step affects the barrier energy shift. A weaker positive correlation was found with the O1–H2 bond length, indicating, as anticipated, that activation of the carbonyl O1 atom—by decreasing the Asp_{40}–substrate distance—also lowers the reaction barrier.

Given the catalytic role of electrostatics in KSI, Hennefarth and Alexandrova investigated the electric field itself, $\boldsymbol{E}(\boldsymbol{r})$, in the KSI active site using both point and regional properties [25]. Here, the set of systems included those exposed to oriented EEFs, and also two 3-chlorotyrosine KSI mutants with respectively higher and lower catalytic activity than wild KSI. They found that the electric field magnitude, $|\boldsymbol{E}(\boldsymbol{r})|$, at the O2–H1, C2–H1, and C1=O1 bond CPs correlated strongly with the change in reaction barrier, but only for the wild KSI structures; KSI-Y^{32} and KSI-Y^{57} were outliers to this trend. These observations were taken to indicate that the mechanism by which the KSI mutants enhance/hinder catalysis is different than that due to EEFs. Furthermore, the correlation at the carbonyl bond CP showed a nearly constant relationship between $|\boldsymbol{E}(\boldsymbol{r})|$ and reaction barrier energy.

Hennefarth and Alexandrova also conducted a regional electric field curvature analysis within two separate rectilinear volumes, one containing the carbonyl C1=O1 atoms, and the other containing

[1] Using the atomic numbering in the present manuscript

the C2–H1$\cdots$O2 atoms of the reaction site. By evaluating the total curvature along $\boldsymbol{E}(\boldsymbol{r})$ streamlines within each volume, they generated histograms that reflect the relative occupations of high and low curvature regions—a regional $\boldsymbol{E}(\boldsymbol{r})$ fingerprint. The corresponding volumes of multiple systems could then be compared by computing the corresponding histogram distances, thus providing a scalar similarity metric also useful for statistical evaluation.

Using this similarity metric, Hennefarth and Alexandrova found that the $\boldsymbol{E}(\boldsymbol{r})$ curvature about the carbonyl bond had a stronger correlation with reaction barrier than that of the reaction site, with 3-chlorotyrosine mutants included in the analysis. This result is counter to the results from point properties (and those of Fuller *et al.*) that the strongest correlations occur in the reaction site rather than within the substrate. The regional results indicate that activation of the carbonyl enhances the reaction rate, where point-based analysis results emphasize changes at the deprotonation site. That is, a regional approach seems to better reveal the underlying chemistry at work common to both the EEF and mutant KSI systems [4, 35].

2.3 The chemical bonding structure of the charge density

Correlations between energy related properties and local charge density metrics abound. However, the assumptions that such relationships exist, and if they do that they are broadly applicable, is questionable, as the local energy of points, lines and arbitrary volumes is ill defined. Our approach minimizes this concern by building on the Quantum Theory of Atoms in Molecules (QTAIM) and considering only volumes over which energy is well-defined [36, 37].

In its standard form, QTAIM is used to locate the boundaries of the "atoms in molecules," aka atomic basins. In addition to possessing unambiguous energies, volumes, and charges, these atoms may be characterized by their topology, which, in turn, is described by zero-, one-, and two-dimensional topological $\rho(\boldsymbol{r})$ features including: critical points (CPs) designated as nuclear, bond, ring, or cage type; bond paths; and inter-atomic surfaces respectively.

That atomic basins have a well-defined energy results from their satisfaction of a zero flux (of the charge density gradient) boundary condition. For an arbitrary region in $\rho(\boldsymbol{r})$, one may calculate the average regional kinetic energy using the gradient or Laplacian forms of the quantum mechanical kinetic energy operator, but these values will not match one another. Over a region bounded by zero-flux surfaces, however, these values will agree, and hence the regional energy of an atomic basin is unambiguous [36].

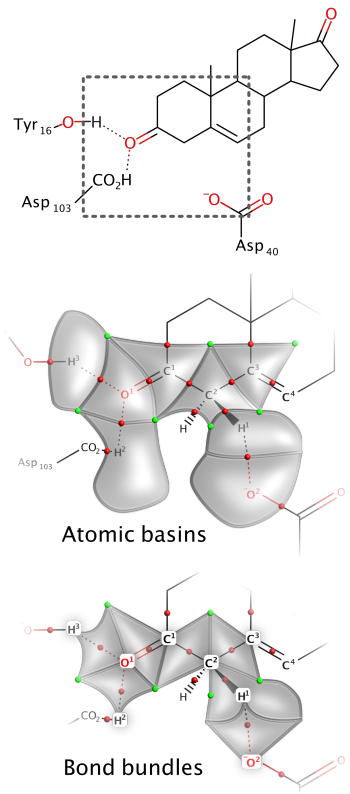

Figure 4: Cartoon depictions of the atomic basins and bond bundles analyzed in this study. Red and green spheres represent bond and ring CPs respectively.

Bond bundle analysis is an extension of QTAIM that recognizes a further partitioning of atomic basins into the smallest regions bounded by zero-flux surfaces called differential gradient bundles (dGBs) [38, 39]. To each dGB there corresponds an unambiguous energy, and an atomic basin can be decomposed into dGBs to produce a continuous and "well-defined energy space." The topology of this space reveals precise boundaries between intra-atomic regions of charge accumulation called bond wedges. Bond wedges of adjacent atoms then combine to form bond bundles [29, 40].

Figure 4 illustrates the eight atomic basins and seven bond bundles considered in this study, as well as the bond and ring CPs that lie along or interior to their boundaries. See the supplemental

information for more realistic, three-dimensional representations of these features. We will appeal to this sort of abstract representation of bond bundles for the remainder of this manuscript. Each has a set of properties commonly associated with a chemical bond, such as an energy and a number of electrons, which, when taken over all bonds in a system, recover the system energy and electron count. In addition to these common bond-like properties, geometry related properties may be determined for a bond wedge including: its volume, its normalized solid angle, its total (or average) geometric curvature, and its total (or average) geometric torsion. The results in the supplemental information include these and other properties for bond wedges, bond bundles, and atomic basins. For illustrative purposes we will include in our analysis the bond wedge solid angle (α), which is the percent area of the nucleus-centered reference sphere occupied by the bond wedge. For example, in a methane molecule, each bond wedge on the C atom would have a solid angle equal to ¼. Like atomic basins, bond bundles have precise, non-overlapping boundaries that combine to fill all space.

3 Results and discussion

3.1 KSI charge density response to a catalyzing EEF

To illustrate the concrete nature of bond bundle properties, we begin by inspecting $\rho(\boldsymbol{r})$ redistribution in the KSI active site due to a catalyzing uniform EEF of magnitude $10^{\mathrm{MV/cm}}$. Table 1 contains regional electron counts for atomic basins, bond bundles, and bond wedges in the KSI active site, as well as their change due to the catalyzing r- EEF. These regional property changes are graphically depicted in Figure 5, where regions are shaded orange or blue (with hash lines) to indicate EEF-induced $\rho(\boldsymbol{r})$ accumulation or depletion respectively. See the supplemental information for similar tables for all five systems, for ten different regional properties.

The KSI active site response to the EEF is nonuniform, and the bond bundle perspective of this response simplifies its interpretation. The field activates the carbonyl O atom (O1), but its primary effect is to redistribute charge consistent with the assumed reaction mechanism. The activation of O1 is evidenced by the accumulation of charge in its atomic basin (Figure 5; left). However, the charge redistribution within the atomic basin is more informative. The center frame of Figure 5 reveals charge accumulation in the O1$\cdots$H2 and O1$\cdots$H3 bond bundles as a consequence of charge depletion in the O1=C1 bond bundle. Still more pronounced is the charge redistribution occuring

Table 1: Regional electron counts in the KSI active site with (EEF) and without (NEF) an applied external electric field of $10^{\mathrm{MV}/\mathrm{cm}}$ pointing from the O nuclear position to the C; the r- direction. Unnumbered atoms were not included in the study. All regions are truncated at the $\rho = 0.001$ isosurface. Complete gradient bundle integration tables are available in the SI.

	Electron count (ρ) [e]			
Atomic basin decomposition	NEF	EEF	Δ	%Δ
C1	5.15	5.19	0.035	0.67
C2	6.21	6.19	-0.021	-0.33
C3	6.18	6.25	0.073	1.18
H1	0.86	0.85	-0.017	-1.92
H2	0.37	0.37	-0.001	-0.22
H3	0.38	0.37	-0.013	-3.46
O1	9.25	9.26	0.013	0.14
O2	9.32	9.33	0.005	0.05
Total	**37.72**	**37.80**	**0.074**	**0.20**
Bond bundle decomposition	NEF	EEF	Δ	%Δ
C1 — C bond wedge	2.05	2.01	-0.040	-1.93
C1 — C2 bond bundle	3.44	3.52	0.089	2.58
↪ *C1 bond wedge*	*2.07*	*2.16*	*0.084*	*4.07*
↪ *C2 bond wedge*	*1.36*	*1.37*	*0.004*	*0.31*
C1 — O1 bond bundle	3.36	3.35	-0.009	-0.28
↪ *C1 bond wedge*	*1.03*	*1.02*	*-0.010*	*-0.99*
↪ *O1 bond wedge*	*2.33*	*2.33*	*0.001*	*0.04*
C2 — H bond wedge	1.63	1.57	-0.051	-3.16
C2 — C3 bond bundle	3.21	3.17	-0.042	-1.31
↪ *C2 bond wedge*	*1.57*	*1.56*	*-0.004*	*-0.25*
↪ *C3 bond wedge*	*1.65*	*1.61*	*-0.038*	*-2.32*
C2 — H1 bond bundle	2.47	2.48	0.013	0.52
↪ *C2 bond wedge*	*1.65*	*1.68*	*0.030*	*1.84*
↪ *H1 bond wedge*	*0.81*	*0.80*	*-0.018*	*-2.17*
C3 — C bond wedge	1.77	1.84	0.073	4.15
C3 — C bond wedge	2.77	2.80	0.038	1.37
H1 — O2 bond bundle	3.66	3.62	-0.046	-1.25
↪ *H1 bond wedge*	*0.05*	*0.05*	*0.001*	*2.15*
↪ *O2 bond wedge*	*3.61*	*3.57*	*-0.047*	*-1.30*
H2 — Asp_{103} bond wedge	0.33	0.33	0.000	0.12
H2 — O1 bond bundle	3.54	3.54	0.005	0.13
↪ *H2 bond wedge*	*0.04*	*0.03*	*-0.001*	*-3.46*
↪ *O1 bond wedge*	*3.50*	*3.51*	*0.006*	*0.17*
H3 — Tyr_{16} bond wedge	0.32	0.30	-0.022	-6.77
H3 — O1 bond bundle	3.47	3.48	0.014	0.42
↪ *H3 bond wedge*	*0.06*	*0.07*	*0.009*	*14.66*
↪ *O1 bond wedge*	*3.41*	*3.41*	*0.006*	*0.17*
O2 — Asp_{40} bond wedge	2.11	2.11	-0.005	-0.24
O2 lone pair wedge	3.60	3.65	0.057	1.58
Total	**37.72**	**37.80**	**0.074**	**0.20**

at the other end of the conjugated system, interior to the substrate. The C1–C2 bond bundle, which is believed to increase its bond order from single to double in the deprotonation step, accumulates nearly 0.09 electrons in response to the field, offset by decreases in the carbonyl bond and more so

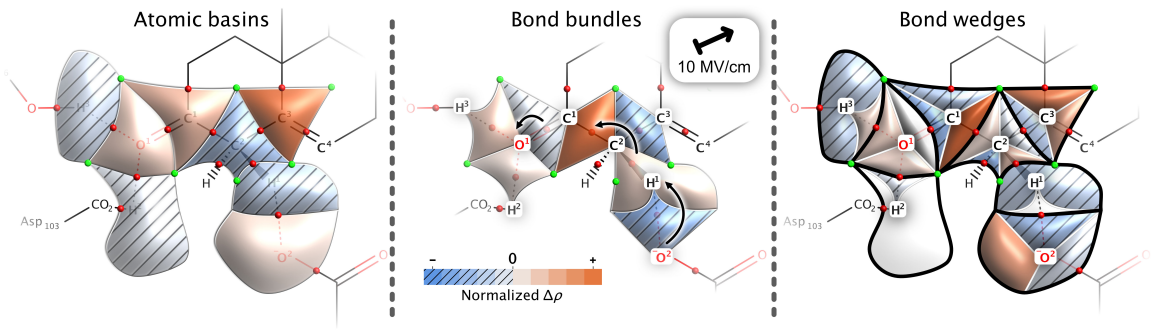

Figure 5: The atomic basins, bond bundles, and bond wedges of KSI (left, middle, and right respectively) shaded according to the changes in their regional electron count due to a $10^{\mathrm{MV/cm}}$ oriented EEF, which are listed in Table 1. The center image includes the electron-pushing arrows of the deprotonation reaction step.

in the C2–C3 bond. At the reaction site, the C2–H1 bond, which is "broken" in the deprotonation step, accumulates charge due to the EEF, while the incipient O2$\cdots$H1 bond loses charge, seemingly the reverse of the anticipated electron motion.

Inspection of the bond wedge values (Figure 5; right), resolves the apparently anomaly. The increase in the C2–H1 bond bundle electron count is due to the contribution of the C2 atom. The H1 bond wedge component of the C2–H1 bond decreases by 0.018 electrons. Because the H1 atom's other bond wedge, corresponding to the O2$\cdots$H1 bond, only increases by 0.001 electrons, we conclude that the remaining 0.017 electrons—the amount lost by the H1 atomic basin—is transferred to the C2 atom rather than redistributed within the H1 atom. That is, shared charge density in the C2–H1 bond was lost by the H1 atom, responsible for at least half of the charge density gained in the corresponding C2 bond wedge. Furthermore, given the much lower electron counts of the O-bonded H atoms—around $0.37e$ in this case—we posit that the H1 atom, at $0.86e$, loses roughly half an electron during its abstraction to Asp_{40}. The EEF-induced decrease of $0.17e$ constitutes over a third of the necessary H1 atomic charge depletion as dictated by the reaction, so here too the $\rho(\boldsymbol{r})$ response to the EEF appears to facilitate deprotonation.

The electron motion determined via gradient bundle analysis recovers and quantifies the traditionally assumed electron motion in unprecedented detail. Still, we note that atomic basins and bond bundles are merely different unions of bond wedges, each providing its own chemical perspective. By construction, changes to bond wedge $\rho(\boldsymbol{r})$ must combine to give the atomic basin or bond bundle changes. Yet owing to their distinct underlying language and associated concepts and models, a very different interpretative process unfolds depending on which is taken to be the irreducible building

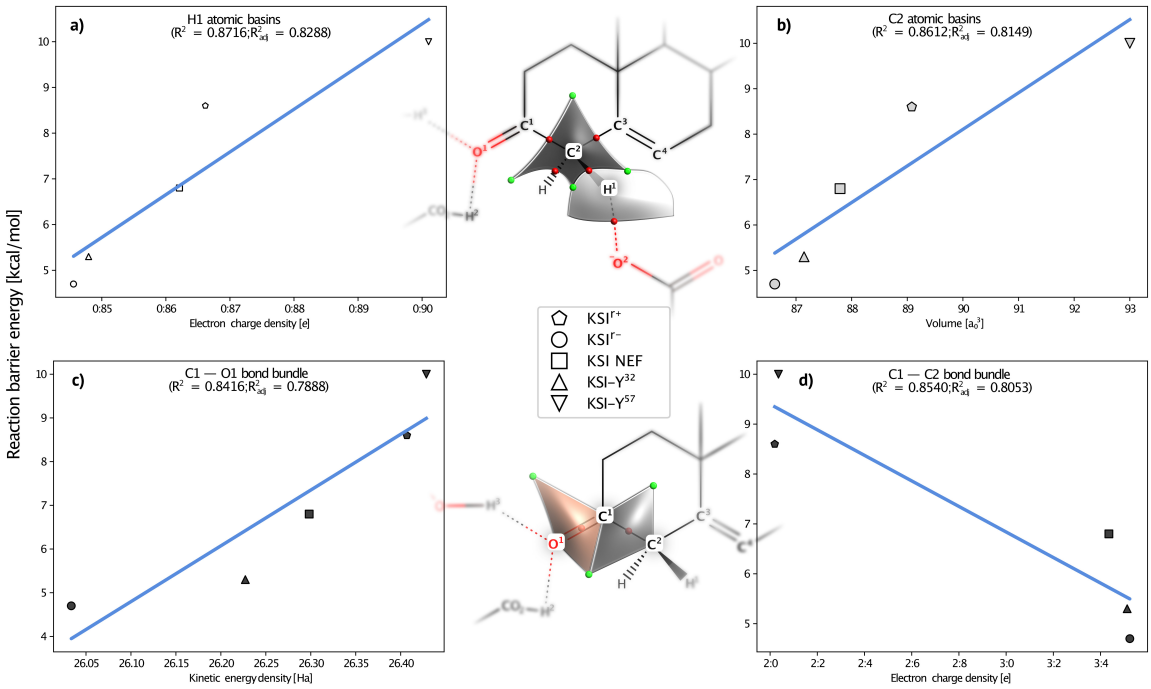

Figure 6: Sampling of atomic basin and bond bundle properties correlated against KSI-catalyzed isomerization reaction barrier energy. Center: Schematic representation of the atomic basins (top) and bond bundles (bottom) shown. Sides: Plots of regional properties vs barrier energy. Full sets of plots used to generate correlations presented in this manuscript are available in the SI.

block of charge density.

3.2 KSI catalytic enhancement and inhibition

While the direct inspection of regional properties can be useful for comparison between small numbers of systems, as above, it can become convoluted with larger datasets or multiple perturbations. As in References 25 and 26, we next take a statistical approach, checking for correlations between the property of interest (system energy in this case) and regional properties, across the five systems: wild type KSI (a.k.a. NEF), EEF-enhanced KSI;$^{r-}$ EEF-inhibited KSI;$^{r+}$ enhanced mutant KSI-Y;^{32} and inhibited mutant KSI-Y.^{57}

Figure 6 shows a selection of some of the fits of reaction barrier height as a function of different gradient bundle condensed properties (see the supplemental information for the complete set of plots for all systems). Atomic basin correlations were strongest for the C2 and H1 atoms. Specifically, the electronic population of the H1 atom correlates positively with reaction barrier, as does the atomic volume of C2. The bond bundle picture, however, indicates that property shifts within the

substrate play an important role, as chemically anticipated. In this case, positive correlation of the O1=C1 bond kinetic energy and negative correlation of the C1–C2 bond population together indicate that, to lower the reaction barrier, charge should increase in the C1–C2 bond, and kinetic energy should decrease in the C1–O1 bond (thus increasing total energy, weakening the carbonyl bond and activating the O atom), in agreement with results in the previous section.

As there are a number of regional properties that can be calculated for bond bundles, bond wedges, and atomic basins, it is helpful to simplify and plot multiple correlation coefficients simultaneously, to see at once how *e.g.* volume and energy each correlate, and to access a more immediate chemical interpretation. Inspired graphically by Reference 41, we have included correlations of regional $\rho(\boldsymbol{r})$ along with regional volume (V), kinetic energy (T), and solid angle (α; Section 2.3) as bar charts in Figure 7. Regions are sorted according to the reaction barrier correlations of ρ, which is also used to shade representative regions as in Figure 5. Note that the shading has opposite meaning between the two figures, in regards to energetic significance. In Figure 7 a blue-hashed region anti-correlates with reaction barrier energy, so an increase in regional properties should lower the reaction barrier. Unlike in Figure 5, where an orange region was one in which $\rho(\boldsymbol{r})$ increased in response to a catalyzing EEF.

In this case, the rate enhancement of the reaction in the KSI active site, resulting from applied electric fields or active-site atomic substitution, is achieved by redistributing charge density between bond bundles in a way that, again, closely resembles our mechanistic understanding of the reaction. Specifically, the C1–C2 bond most anti-correlates with reaction barrier energy, indicating that promoting (or hindering) its transition from single to double bond generally lowers (or raises) the reaction barrier. The O1=C1 and O1$\cdots$H3 bond bundles respectively correlate and anti-correlate with barrier height, indicating that activation of the O atom—or at least increasing its lone pair density and decreasing the carbonyl bond density—lowers the barrier. At the deprotonation site, the C2–H1 bond properties anti-correlate with barrier height, suggesting paradoxically that increasing the property content of the "breaking" bond facilitates its own breaking. Altogether, the bond bundle property correlations seem to indicate the same underlying catalytic charge density shifts as those resulting from an applied EEF, including the reversed behavior at the deprotonation site. Here the results indicate a structure property relationship between reactant state substrate bond bundle properties and the barrier height of the KSI-catalyzed reaction, regardless of the source of bond bundle property perturbation.

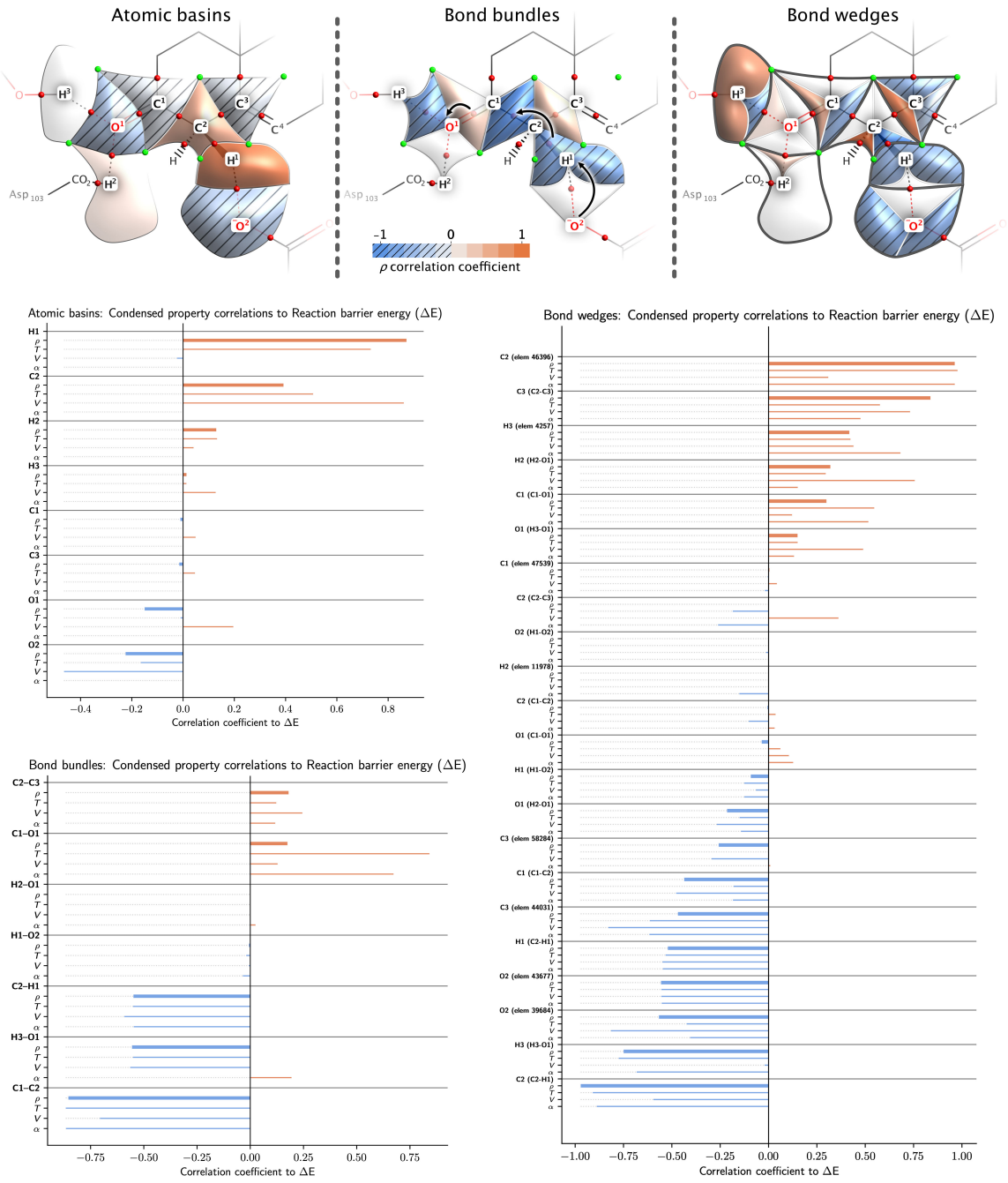

Figure 7: Atomic basin, bond bundle, and bond wedge (top; left to right) property correlations with reaction barrier energy, signed as positive or negative to indicate correlation and anti-correlation. Above are cartoon, schematic depictions of the overlaid on the Lewis representation of the active site, with electron pushing arrows in the center pane denoting the deprotonation reaction step from Scheme 1. Regions are shaded above, and sorted in the plots below, according to the sign and magnitude of their electron population (ρ) correlations with reaction barrier. The regional kinetic energy (T), volume (V), and normalized solid angle (α) are plotted as well. Complete multi-variable correlation bar charts are available in the SI.

Another conclusion, similar in part to the previous section, can be arrived at from the inspection of atomic basin correlations. In this case, the C2 and H1 atoms at the deprotonation site correlate with barrier height, indicating their combined atomic properties should be lowered—as resulted from the applied r- field—in order to facilitate deprotonation. The O1 atom anti-correlates, suggesting again that it should be activated via accumulating charge density, but only slightly. However, while the conjugated carbon system experienced the greatest amount of inter-atomic $\rho(\boldsymbol{r})$ redistribution due to the EEF (Figure 5), the C1 and C3 atomic properties show almost no correlation with reaction barrier. Instead, the H1 and C2 atoms most strongly correlate. This disparity suggests that the atomic basin $\rho(\boldsymbol{r})$ redistribution accompanying the catalytic r- EEF is not generally indicative of a catalytic effect. On the other hand, the r- EEF-induced bond bundle redistribution seems quite indicative of the general behavior.

Indeed, the (anti)similarity between bond bundle correlations and EEF-induced bond bundle property shifts is stark. With very few exceptions, regions of $\rho(\boldsymbol{r})$ accumulation due to the r- field are those that anti-correlate with reaction barrier. Likewise, regions of $\rho(\boldsymbol{r})$ depletion due to the field correlate positively with reaction barrier. Additionally, the C1–C2 bond bundle, which experienced the greatest increase in $\rho(\boldsymbol{r})$ due to the EEF, strongly anti-correlates with barrier height. Given that the r- system was included in the regional correlations, and that it is the most rate-enhancing system in the (small) sample, it is no surprise that it should be represented in the resulting correlations. However, as noted above, atomic basin regional correlations share less similarity with their r- field-induced redistribution in KSI.

A final and somewhat unexpected similarity to the results of the previous section is the additivity of bond wedge property correlations to predict those of bond bundles and atomic basins. For example, the two H3 bond wedges strongly correlate and anti-correlate respectively, and the H3 atomic basin as a whole has nearly zero correlation, as if its bond wedges combined deconstructively to give the whole. The same deconstructive behavior is apparent in the C1 and C3 atoms, while the H1 atom is clearly an outlier to this trend. Bond wedge correlations combine to predict those of bond bundles in a similar way, and in this case without exception; the correlation of each bond bundle appears to be the sum of its bond wedge correlations. While gradient bundle properties are definitionally additive, it cannot be said that gradient bundle energetic significance is additive. Here we have the H1 atom—whose bond wedge correlations would sum to negative rather than positive atomic basin correlation—as our proof by contradiction *against* such additivity in general.

Regardless, bond wedge regional energetic significance does seem to typically combine to predict bond bundle significance.

Regarding the nearly uniform agreement between the correlations of different regional properties with reaction barrier energy, we have previously observed that the regional volume, kinetic energy, and solid angle tend to correlate strongly with the charge density, at least in organic systems [29]. Hence, it is unsurprising that these properties should yield similar correlations with respect to reaction barrier height, as is clearly the general case in KSI. Disagreement between reaction barrier-property correlations for a particular region indicates an underlying lack of correlation between the properties themselves across the set of systems. This assertion can be confirmed by inspecting the correlations among regional properties. Figure 8 shows correlation matrices between the four regional properties for a selection of gradient bundles (one matrix per gradient bundle), where the size and color of each square in a matrix indicates the correlation between the properties at its corresponding row and column (see the supplemental information for correlation matrices for all gradient bundles and properties). Within the C1–O1 bond bundle in Figure 7, for example, kinetic energy (T) and solid angle (α) correlate more strongly with reaction barrier than do charge density (ρ) and volume (V), and by similar amounts—$R^2 \approx 0.7$ for T and α and $R^2 \approx 0.2$ for ρ and V. In Figure 8 we see that within the C1–O1 bond bundle (matrix in center column, bottom row), ρ and V correlate strongly with each other but weakly with T and α, and that the reverse is true; T and α correlate strongly with each other but weakly with ρ and V. Hence the difference in reaction barrier height correlations of these regional properties stems from the fact that they respond differently to the applied EEFs than to amino acid atomic substitution in the KSI active site.

Furthermore, this is consistent for all regions in the study. The C1–C2 bond bundle, for example, has very similar anti-correlation to reaction barrier height for all four properties ($R^2 \approx 0.8$), and in Figure 8 we see they all strongly correlate with each other as well. Next, the H1 atomic basin has strong ρ and T barrier correlation ($R^2 \approx 0.8$) but weak V anti-correlation ($R^2 \approx 0.02$), and indeed ρ and T correlate strongly with each other and weakly with V. The C2 atomic basin is similar in both respects to H1, but less pronounced. Finally, the two C2–H bond wedges are a particularly good example because they experience the strongest overall correlations to reaction barrier height, and both correlate more weakly with V ($R^2 \approx 0.55, 0.31$) than with ρ, T, or α ($R^2 \approx 0.89$ to 0.98). Likewise, in both C2–H bond wedges, ρ, T, and α correlate strongly with each other and weakly with V. Because the correlation among regional properties appears to be closely tied to their relative

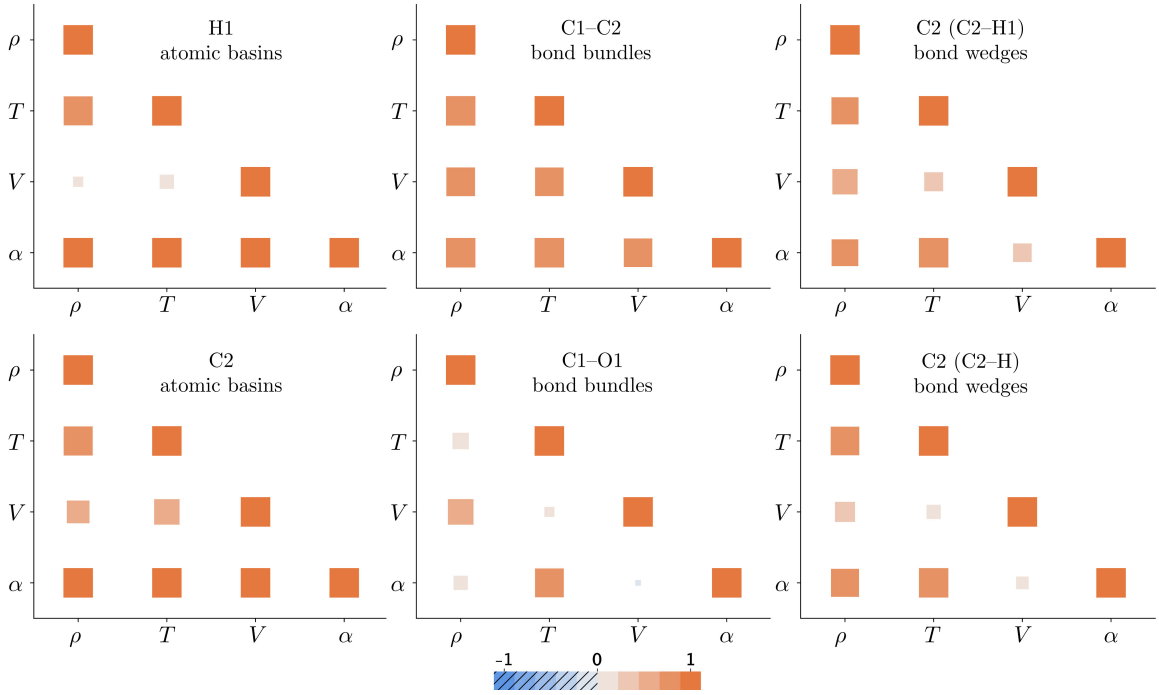

Figure 8: Correlation matrices showing property correlations within a selection of gradient bundles. Electron density (ρ), kinetic energy (T), volume (V), and solid angle (α) are included. For example, the correlation between ρ and α in the H1 atomc basin across all five systems, indicated at the (α, ρ) position in the top-left plot, is stronger than the correlation between ρ and V, which has a smaller, lighter symbol. Full sets of correlation matrices are provided in the SI.

energetic significance, we speculate that different types of system changes (*e.g.* an applied EEF vs. amino acid mutation) enhance catalysis through different mechanisms that affect and utilize some properties more than others within a given region. Further, we speculate that weak correlation between a region's properties (*e.g.* the C1–O1 bond bundle, where T and α correlate strongly with each other but weakly with ρ and V) indicates the region is used by these different mechanisms in functionally different ways. Conversely, strong correlation between a region's properties, *together with strong correlation to reaction barrier height* (*e.g.* the C1–C2 bond bundle) indicates that the region has similar energetic significance and catalytic functionality regardless of the type of system change, *i.e.* that it more fundamentally underlies the catalysis.

Overall, in regards to the mechanism of KSI catalytic augmentation, this statistical use of bond bundle property analysis leads us to chemically similar conclusions to those of direct inspection of EEF-induced bond bundle property redistributions from the previous section. Activation of the substrate O atom, and charge accumulation in the C1–C2 bond bundle, as result from the catalyzing r- EEF, here indicate a more general structure-property relationship between KSI active site bond bundle properties and reaction barrier height. Correlations of reaction barrier energy to bond bundle regional properties largely recover the known redistribution of the catalyzed chemical reaction depicted with electron-pushing arrows. The bond bundle analysis results invite interpretations firmly within existing bonding concepts. In this way, our conclusions were not arrived at using chemical intuition like a rosetta stone to decipher raw data. Rather, because the raw data are explicitly descriptive of bond properties, even the most basic sort of direct inspection and statistical analysis, in this case, recovered our chemical intuition.

4 Conclusion

The pursuit of rational, computer-aided artificial enzyme design requires a robust understanding of the chemical reactions catalyzed, down to the level of individual atom and bond energies. Here we have presented one method of directly accessing the energies and energy-mediated properties of real-space bonding regions in any chemical system, applied to the specific problem of KSI catalysis. We inspected the redistribution of $\rho(\boldsymbol{r})$ due to a catalyzing EEF, qualitatively and quantitatively observed bond transitions similar to those of the conventionally assumed reaction mechanism, and found that the catalyzing field was that which shifts $\rho(\boldsymbol{r})$, non-uniformly, in the forward reaction

direction. We also found that correlations between reaction barrier energies and bond bundle properties recovered a similar picture of the expected charge rearrangement.

The gradient bundle properties presented here, together with the larger integration tables contained in the supplementary information, are but a small sample of what can currently be calculated. We have only begun to investigate the statistical and conceptual significance of this extensive set of properties. While we expect direct inspection and graphical depictions to remain useful tools for chemical interpretation, our results demonstrate promise for applications with machine learning algorithms. A concern with machine learning is that the resulting models may be so abstract as to be unapproachable using physical chemical intuition. Indeed, the more conceptual distance between the input and output of a machine learning model, the greater the conceptual gap one must span to understand the physical significance of its underlying correlations. To train a model to predict system energies, and one that can be interpreted in the language of chemistry, it seems doubly advantageous to use input data that explicitly include the precise energy of the bonds in the system. Thus gradient bundle regional properties show promise for machine learning applications.

Constructing a complete, descriptive network of enzyme $\rho(\boldsymbol{r})$ structure-property relationships, such that local changes in $\rho(\boldsymbol{r})$ could be used to accurately predict catalytic rate enhancement, will be a formidable task owing to the lack of underlying energetic additivity between the independent properties of enzymes [31]. Bond bundles do possess spatial and energetic additivity, are uniquely defined in any chemical system, and their analysis appears to naturally leverage our hard won understanding of chemical bonding. Furthermore, in this case the correlation of bond wedge properties with rate enhancement did, in fact, appear to be additive, so there is a readily quantifiable sense in which catalyzing features may have underlying energetic additivity. Bond wedge and bond bundles are thus attractive tools for identifying, measuring, and contextualizing $\rho(\boldsymbol{r})$ and other property redistribution that accompanies and underlies enzymatic catalysis.

Methods

All *ab-initio* calculations were performed using the ADF package of The Amsterdam Modeling Suite [42–44]. Relaxed system geometries were obtained with initial coordinates from References 26 and 25 as mentioned above. Optimization of all five systems was performed using a triple-ζ STO all-electron basis set with one polarization function [45], with the Minnesota'06-2X XC energy density

functional [46, 47] and "good" numerical integration quality. The NEF system relaxation also included implicit COSMO solvation [48, 49] using Allinger solvent radii and a dielectric constant of $\varepsilon = 4.0$. Subsequent single-point calculations were run with the same basis set and functional, with the same COSMO settings now used for all systems. All applied electric fields were of magnitude $10^{\mathrm{MV}/\mathrm{cm}}$. The formaldehyde calculation results in Table 1 used a triple-ζ all-electron basis set with the PBE functional [50].

Topological analysis, along with atomic basin and bond bundle/wedge decomposition was performed with the Bondalyzer software suite of the Molecular Theory Group at Colorado School of Mines [51], an add-on to the Tecplot360 visualization package [52]. Statistical analysis was performed in Python, and the MatPlotLib [53] and SeaBorn [54] libraries were used for plotting line/scatter and bar charts respectively. Chemical diagrams were composed in MarvinSketch [55]. Final figures were compiled in Affinity Designer [56].

Acknowledgments

This work was supported by the National Science Foundation grant CHE-1903808, and by the Office of Naval Research grants N00014-05-C-0241 and N00014-10-1-0838.

Supporting information

Supporting information is provided free of charge at (link to SI)

- 3D depictions of some of the regions discussed in the manuscript
- Coordinates and energies of *ab-initio* calculations
- Atomic basin, bond bundle, and bond wedge tabulated integration values *with many more properties than are included in this manuscript*
- Single and multi-variable bar charts of simplified regional property correlations
- Plots of fits of each region and property with reaction barrier energy
- Correlations among regional properties

References

[1] Arieh Warshel. Electrostatic basis of Structure–Function correlation in proteins. *Accounts of Chemical Research*, 14:284–290, 1981.

[2] Arieh Warshel. Electrostatic Origin of the Catalytic Power of Enzymes and the Role of Preorganized Active Sites*. *Journal of Biological Chemistry*, 273(42):27035–27038, October 1998. doi:10.1074/jbc.273.42.27035.

[3] Arieh Warshel, Pankaz K. Sharma, Mitsunori Kato, Yun Xiang, Hanbin Liu, and Mats H. M. Olsson. Electrostatic Basis for Enzyme Catalysis. *Chemical Reviews*, 106(8):3210–3235, August 2006. doi:10.1021/cr0503106.

[4] Matthew R. Hennefarth and Anastassia N. Alexandrova. Advances in optimizing enzyme electrostatic preorganization. *Current Opinion in Structural Biology*, 72:1–8, February 2022. doi:10.1016/j.sbi.2021.06.006.

[5] Rinat Meir, Hui Chen, Wenzhen Lai, and Sason Shaik. Oriented Electric Fields Accelerate Diels–Alder Reactions and Control the endo/exo Selectivity. *ChemPhysChem*, 11(1):301–310, 2010. doi:10.1002/cphc.200900848.

[6] Albert C. Aragonès, Naomi L. Haworth, Nadim Darwish, Simone Ciampi, Nathaniel J. Bloomfield, Gordon G. Wallace, Ismael Diez-Perez, and Michelle L. Coote. Electrostatic catalysis of a Diels–Alder reaction. *Nature*, 531(7592):88–91, March 2016. doi:10.1038/nature16989.

[7] Sason Shaik, Debasish Mandal, and Rajeev Ramanan. Oriented electric fields as future smart reagents in chemistry. *Nature Chemistry*, 8(12):1091–1098, December 2016. doi:10.1038/nchem.2651.

[8] Zhanfeng Wang, David Danovich, Rajeev Ramanan, and Sason Shaik. Oriented-External Electric Fields Create Absolute Enantioselectivity in Diels–Alder Reactions: Importance of the Molecular Dipole Moment. *Journal of the American Chemical Society*, 140(41):13350–13359, October 2018. doi:10.1021/jacs.8b08233.

[9] Chao Wang, David Danovich, Hui Chen, and Sason Shaik. Oriented External Electric Fields:

Tweezers and Catalysts for Reactivity in Halogen-Bond Complexes. *Journal of the American Chemical Society*, 141(17):7122–7136, May 2019. doi:10.1021/jacs.9b02174.

[10] Ming-Xia Zhang, Hong-Liang Xu, and Zhong-Min Su. The directions of an external electric field control the catalysis of the hydroboration of C–O unsaturated compounds. *RSC Advances*, 9(50):29331–29336, September 2019. doi:10.1039/C9RA03895G.

[11] Yaping Zang, Qi Zou, Tianren Fu, Fay Ng, Brandon Fowler, Jingjing Yang, Hexing Li, Michael L. Steigerwald, Colin Nuckolls, and Latha Venkataraman. Directing isomerization reactions of cumulenes with electric fields. *Nature Communications*, 10(1):4482, October 2019. doi:10.1038/s41467-019-12487-w.

[12] Edoardo Jun Mattioli, Andrea Bottoni, Francesco Zerbetto, and Matteo Calvaresi. Oriented External Electric Fields Affect Rate and Stereoselectivity of Electrocyclic Reactions. *The Journal of Physical Chemistry C*, 123(43):26370–26378, October 2019. doi:10.1021/acs.jpcc.9b07358.

[13] Carles Acosta-Silva, Joan Bertran, Vicenç Branchadell, and Antoni Oliva. Kemp Elimination Reaction Catalyzed by Electric Fields. *ChemPhysChem*, 21(4):295–306, 2020. doi:10.1002/cphc.201901155.

[14] Thijs Stuyver, David Danovich, Jyothish Joy, and Sason Shaik. External electric field effects on chemical structure and reactivity. *WIREs Computational Molecular Science*, 10(2):e1438, 2020. doi:10.1002/wcms.1438.

[15] Mark Dittner and Bernd Hartke. Globally optimal catalytic fields for a Diels–Alder reaction. *The Journal of Chemical Physics*, 152(11):114106, March 2020. doi:10.1063/1.5142839.

[16] Sason Shaik, David Danovich, Jyothish Joy, Zhanfeng Wang, and Thijs Stuyver. Electric-Field Mediated Chemistry: Uncovering and Exploiting the Potential of (Oriented) Electric Fields to Exert Chemical Catalysis and Reaction Control. *Journal of the American Chemical Society*, 142(29):12551–12562, July 2020. doi:10.1021/jacs.0c05128.

[17] Fengyi Liu and Minjuan Liu. An Intuitive Electric-field Contribution Decomposition Model for Chemical Processes and Its Applications on Diels-Alder Reactions. *Chemical Research in Chinese Universities*, 36(6):1241–1248, December 2020. doi:10.1007/s40242-020-0143-x.

[18] Song Yu, Pascal Vermeeren, Trevor A. Hamlin, and F. Matthias Bickelhaupt. How Oriented External Electric Fields Modulate Reactivity. *Chemistry – A European Journal*, 27(18):5683–5693, 2021. doi:10.1002/chem.202004906.

[19] S. Shaik, D. Danovich, K. D. Dubey, and T. Stuyver. The Impact of Electric Fields on Chemical Structure and Reactivity. In *Effects of Electric Fields on Structure and Reactivity*, pages 12–70. The Royal Society of Chemistry, March 2021. doi:10.1039/9781839163043-00012.

[20] Nadia G. Léonard, Rakia Dhaoui, Teera Chantarojsiri, and Jenny Y. Yang. Electric Fields in Catalysis: From Enzymes to Molecular Catalysts. *ACS Catalysis*, 11(17):10923–10932, September 2021. doi:10.1021/acscatal.1c02084.

[21] Wei-Wei Wang, Fu-Lin Shang, and Xiang Zhao. Switchable (2 + 2) and (4 + 2) Cycloadditions on Boron Nitride Nanotubes under Oriented External Electric Fields: A Mechanistic Study. *The Journal of Organic Chemistry*, 86(5):3785–3791, March 2021. doi:10.1021/acs.joc.0c02590.

[22] Timothy Wilson and Mark Eberhart. A Bond Bundle Case Study of Diels-Alder Catalysis Using Oriented Electric Fields. January 2022. doi:10.26434/chemrxiv-2021-17wpx-v2.

[23] Valerie Vaissier Welborn, Luis Ruiz Pestana, and Teresa Head-Gordon. Computational optimization of electric fields for better catalysis design. *Nature Catalysis*, 1(9):649–655, September 2018. doi:10.1038/s41929-018-0109-2.

[24] Shahin Sowlati-Hashjin, Mikko Karttunen, and Chérif F. Matta. Manipulation of Diatomic Molecules with Oriented External Electric Fields: Linear Correlations in Atomic Properties Lead to Nonlinear Molecular Responses. *The Journal of Physical Chemistry A*, 124(23):4720–4731, June 2020. doi:10.1021/acs.jpca.0c02569.

[25] Matthew R. Hennefarth and Anastassia N. Alexandrova. Direct Look at the Electric Field in Ketosteroid Isomerase and Its Variants. *ACS Catalysis*, 10(17):9915–9924, September 2020. doi:10.1021/acscatal.0c02795.

[26] Jack Fuller, Tim R. Wilson, Mark E. Eberhart, and Anastassia N. Alexandrova. Charge Density in Enzyme Active Site as a Descriptor of Electrostatic Preorganization. *Journal of Chemical Information and Modeling*, 59(5):2367–2373, May 2019. doi:10.1021/acs.jcim.8b00958.

[27] Timothy R. Wilson, Anastassia N. Alexandrova, and M. E. Eberhart. Electron Density Geometry and the Quantum Theory of Atoms in Molecules. *The Journal of Physical Chemistry A*, 125(50):10622–10631, December 2021. doi:10.1021/acs.jpca.1c09359.

[28] Travis E Jones and Mark E Eberhart. The Bond Bundle in Open Systems. *International Journal of Quantum Chemistry*, 110(8):1500–1505, 2010. doi:10.1002/qua.22270.

[29] Timothy R. Wilson, Malavikha Rajivmoorthy, Jordan Goss, Sam Riddle, and Mark E. Eberhart. Observing the 3D Chemical Bond and its Energy Distribution in a Projected Space. *ChemPhysChem*, 20(24):3289–3305, 2019. doi:10.1002/cphc.201900962.

[30] Daniel A. Kraut, Paul A. Sigala, Brandon Pybus, Corey W. Liu, Dagmar Ringe, Gregory A. Petsko, and Daniel Herschlag. Testing Electrostatic Complementarity in Enzyme Catalysis: Hydrogen Bonding in the Ketosteroid Isomerase Oxyanion Hole. *PLOS Biology*, 4(4):e99, March 2006. doi:10.1371/journal.pbio.0040099.

[31] Daniel Herschlag and Aditya Natarajan. Fundamental Challenges in Mechanistic Enzymology: Progress toward Understanding the Rate Enhancements of Enzymes. *Biochemistry*, 52(12):2050–2067, March 2013. doi:10.1021/bi4000113.

[32] Stephen D. Fried, Sayan Bagchi, and Steven G. Boxer. Extreme electric fields power catalysis in the active site of ketosteroid isomerase. *Science*, 346(6216):1510–1514, December 2014.

[33] Arieh Warshel, Pankaz K. Sharma, Zhen T. Chu, and Johan Åqvist. Electrostatic Contributions to Binding of Transition State Analogues Can Be Very Different from the Corresponding Contributions to Catalysis: Phenolates Binding to the Oxyanion Hole of Ketosteroid Isomerase. *Biochemistry*, 46(6):1466–1476, February 2007. doi:10.1021/bi061752u.

[34] Gregory M. Vath, Cathleen A. Earhart, James V. Rago, Michael H. Kim, Gregory A. Bohach, Patrick M. Schlievert, and Douglas H. Ohlendorf. The Structure of the Superantigen Exfoliative Toxin A Suggests a Novel Regulation as a Serine Protease,. *Biochemistry*, 36(7):1559–1566, February 1997. doi:10.1021/bi962614f.

[35] Matthew R. Hennefarth and Anastassia N. Alexandrova. Heterogeneous Intramolecular Electric Field as a Descriptor of Diels–Alder Reactivity. *The Journal of Physical Chemistry A*, 125(5):1289–1298, February 2021. doi:10.1021/acs.jpca.1c00181.

[36] R F W Bader, T T Nguyen-Dang, and Per-Olov Löwdin. Quantum Theory of Atoms in Molecules–Dalton Revisited. In *Advances in Quantum Chemistry*, volume Volume 14, pages 63–124. Academic Press, 1981. doi:10.1016/S0065-3276(08)60326-3.

[37] Chérif F Matta and Russell J Boyd. *The Quantum Theory of Atoms in Molecules: From Solid State to DNA and Drug Design*. Weinheim: Wiley-VCH, 2007.

[38] Amanda Morgenstern, Tim Wilson, Jonathan Miorelli, Travis Jones, and M E Eberhart. In Search of an Intrinsic Chemical Bond. *Computational and Theoretical Chemistry*, 1053(0):31–37, 2015. doi:http://dx.doi.org/10.1016/j.comptc.2014.10.009.

[39] Amanda Morgenstern and Mark Eberhart. Bond dissociation energies from the topology of the charge density using gradient bundle analysis. *Physica Scripta*, 91(2):23012, 2016.

[40] Timothy R. Wilson and M.E. Eberhart. Quantum theory of atoms in molecules in condensed charge density space. *Canadian Journal of Chemistry*, 97(11):757–762, July 2019. doi:10.1139/cjc-2019-0086.

[41] Adriano M. Luchi, Roxana N. Villafañe, J. Leonardo Gómez Chávez, M. Lucrecia Bogado, Emilio L. Angelina, and Nelida M. Peruchena. Combining Charge Density Analysis with Machine Learning Tools To Investigate the Cruzain Inhibition Mechanism. *ACS Omega*, 4(22):19582–19594, November 2019. doi:10.1021/acsomega.9b01934.

[42] G te Velde, F M Bickelhaupt, E J Baerends, C Fonseca Guerra, S J A van Gisbergen, J G Snijders, and T Ziegler. Chemistry with ADF. *Journal of Computational Chemistry*, 22(9):931–967, 2001. doi:10.1002/jcc.1056.

[43] C. Fonseca Guerra, J. G. Snijders, G. te Velde, and E. J. Baerends. Towards an order-N DFT method. *Theoretical Chemistry Accounts*, 99(6):391–403, November 1998. doi:10.1007/s002140050353.

[44] ADF 2019.3. SCM, 2019.

[45] E Van Lenthe and E J Baerends. Optimized Slater-type basis sets for the elements 1–118. *Journal of Computational Chemistry*, 24(9):1142–1156, 2003. doi:10.1002/jcc.10255.

[46] Yan Zhao and Donald G. Truhlar. A new local density functional for main-group thermochemistry, transition metal bonding, thermochemical kinetics, and noncovalent interactions. *The Journal of Chemical Physics*, 125(19):194101, November 2006. doi:10.1063/1.2370993.

[47] Yan Zhao and Donald G Truhlar. The M06 suite of density functionals for main group thermochemistry, thermochemical kinetics, noncovalent interactions, excited states, and transition elements: Two new functionals and systematic testing of four M06-class functionals and 12 other function. *Theoretical Chemistry Accounts*, 120(1):215–241, 2008. doi:10.1007/s00214-007-0310-x.

[48] Andreas Klamt. Conductor-like Screening Model for Real Solvents: A New Approach to the Quantitative Calculation of Solvation Phenomena. *The Journal of Physical Chemistry*, 99(7):2224–2235, February 1995. doi:10.1021/j100007a062.

[49] Cory C. Pye and Tom Ziegler. An implementation of the conductor-like screening model of solvation within the Amsterdam density functional package. *Theoretical Chemistry Accounts*, 101(6):396–408, May 1999. doi:10.1007/s002140050457.

[50] John P. Perdew, Kieron Burke, and Matthias Ernzerhof. Generalized Gradient Approximation Made Simple. *Physical Review Letters*, 77(18):3865–3868, October 1996. doi:10.1103/PhysRevLett.77.3865.

[51] Tim R. Wilson and Mark E. Eberhart. Bondalyzer. First Principles Materials Design and Software, October 2021.

[52] Tecplot Inc. Tecplot 360 2013R1. Tecplot Inc., 2013.

[53] J D Hunter. Matplotlib: A 2D graphics environment. *Computing In Science & Engineering*, 9(3):90–95, 2007.

[54] Michael L. Waskom. Seaborn: Statistical data visualization. *Journal of Open Source Software*, 6(60):3021, 2021. doi:10.21105/joss.03021.

[55] Marvin — ChemAxon. https://chemaxon.com/products/marvin.

[56] Affinity Designer – Professional Graphic Design Software. https://affinity.serif.com/en-us/designer/.